

Review

Quantification of Nanomaterial Surfaces

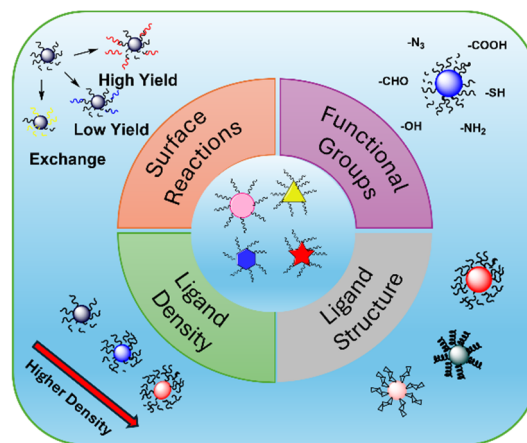
Harshit Kumar and Mingdi Yan *

Department of Chemistry, University of Massachusetts Lowell, 1 University Avenue, Lowell, MA 01854, USA

* Correspondence: Mingdi_Yan@uml.edu

Received: 24 February 2025; Revised: 3 March 2025; Accepted: 5 March 2025; Published: 10 March 2025

Abstract: Quantification of nanomaterial surfaces is critical in the design of nanomaterials with predictable and tailored functions. Nanomaterials exhibit unique surface properties, such as high surface-to-volume ratios and tunable chemistry, which govern their stability, reactivity, and functions in a wide range of applications including catalysis, drug delivery, bioimaging, and environmental remediation. However, quantitative analysis of the nanomaterial surface is challenging due to the inherent heterogeneity, which affects the surface structure, ligand density and presentation. This mini review discusses several important aspects of surface quantification, including ligand structure, ligand density, functional groups, and surface reactions. Traditional analytical methods, such as nuclear magnetic resonance (NMR) spectroscopy, mass spectrometry (MS), and UV-vis spectroscopy, as well as emerging techniques that offer higher spatial resolution and sensitivity are discussed, and examples are given.



Keywords: nanomaterial surface; quantification; ligand structure; surface reactions

1. Introduction

Nanomaterials have gained wide uses in both fundamental research and for applications in catalysis, drug delivery, bioimaging, electronic devices, and energy owing to their extraordinary properties. Many of these applications originate from their surface properties such as high surface area-to-volume ratios and tunable surface chemistry [1,2]. The surface of nanomaterials plays a central role in determining their interactions with the surrounding environment, which directly influences their stability, reactivity, and functional performance [3,4]. Understanding and controlling these surface properties is essential for optimizing nanomaterials for the desired applications.

Nanomaterials are generally capped with ligands, which are molecules or ions that bind to the surface of the nanomaterial. Ligands on the surface of nanomaterials serve a number of important roles. (1) Reducing high-energy nanomaterial surfaces by passivating surface atoms. Without the surface ligands, nanomaterials are prone to aggregate or undergo unwanted reactions as they minimize surface energy [5,6]. (2) Controlling nanomaterial size and shape during synthesis. Surface ligands can influence the nucleation and growth rates, and dictate the final particle size through steric stabilization and surface charge [7]. When ligands preferentially bind to certain crystallographic facets, the facet-specific binding allows for precise control over the structural features of nanomaterials, such as anisotropic shapes and hierarchical assemblies [8–10]. (3) Tuning surface properties of nanomaterials. Through functional groups such as carboxy (-COOH), amine (-NH₂), or azide (-N₃), surface ligands enable further chemical modifications of the nanomaterial to improve the chemical reactivity, environmental stability, and biocompatibility [11]. Detailed understanding of the nanomaterial surfaces is therefore essential for the rational design of nanomaterials with predictable and tailored properties.

Ligands can be introduced to nanomaterial surfaces via non-covalent or coordination interactions, or by covalent bond formation [12,13]. In non-covalent interactions, ligands adhere to nanomaterial surfaces through hydrogen bonding, electrostatic forces, or hydrophobic interactions. For example, ligands such as polymers or



Copyright: © 2025 by the authors. This is an open access article under the terms and conditions of the Creative Commons Attribution (CC BY) license (<https://creativecommons.org/licenses/by/4.0/>).

Publisher's Note: Scilight stays neutral with regard to jurisdictional claims in published maps and institutional affiliations.

long-chain surfactants physisorb onto the nanomaterial surface via multivalent non-covalent interactions, which strengthen the ligand-nanomaterial interface. In coordination interactions, ligands such as amines, phosphines, and carboxylates coordinate with metals via dative bonds. Covalent bond formation provides strong ligand attachment, resulting in stable ligand-nanomaterial interface. Common examples include thiols/disulfides on metal or semiconductor nanomaterials, and silanes on oxide nanomaterials. Additional ligands can be introduced to nanomaterial surface through ligand exchange or post-synthesis modification. In ligand exchange, the original capping ligand is replaced by a ligand having higher affinity for the nanomaterials. For instance, citrate-capped gold nanomaterials can be modified by replacing citrate with thiol ligands, as the S-Au bond is stronger than the ionic citrate-gold interaction. Post-synthesis modification involves covalently conjugating a new ligand to the nanomaterial surface through reactions such as amine-carboxy amidation and azide-mediated click reactions.

However, quantifying nanomaterial surfaces remains a significant challenge due to their inherent heterogeneity. Nanomaterial surfaces often exhibit varying crystalline facets, structural defects, and curvatures, which influence ligand attachment, presentation, density, and reactivity [14,15]. Crystalline facets determine the surface energy, where high energy facets result in stronger ligand binding than low-energy facets, leading to uneven ligand attachments across the surface. Structural defects such as vacancies, dislocations, and grain boundaries are also high-energy sites that can cause ligands to cluster around them and leave other areas under-functionalized [14]. Curvature introduces another complexity [16,17]. On high curvature surfaces, e.g., small nanoparticles, ligands are spaced further apart, resulting in lower packing efficiency. This leads to reduced steric hindrance and enhanced functional group accessibility, potentially enhancing surface reactivity. On the other hand, flat and concave surfaces result in denser ligand packing, which can lead to stronger intermolecular interactions, reduced ligand mobility, and decreased reactivity. Collectively, these characteristics lead to non-uniform surfaces, making it challenging to characterize nanomaterial surfaces especially at the molecular level.

This mini review discusses four aspects of surface quantification: ligand structure, ligand density, functional groups, and surface reactions. We discuss traditional analytical methods such as NMR and UV-vis spectroscopy as they are well-established and widely accessible, as well as chemical assays that are ligand specific. We also discuss advanced analytical techniques that offer enhanced spatial resolution, sensitivity, and the ability to probe nanomaterial surfaces at the single-particle level. Since nanoparticles are the most studied nanomaterials, the terms nanomaterials and nanoparticles will be used interchangeably throughout the discussions.

2. Determination of Ligand Structure

Knowledge of the structure and spatial distribution of surface ligands is an important aspect that directly impacts the stability, reactivity, and functions of nanomaterials. High-resolution transmission electron microscopy (HR-TEM) can determine the crystalline structure of the nanoparticle core and visualize the nanoparticle-ligand interface, but the organic ligand shell often lacks sufficient contrast for its structure to be resolved directly [18]. The state-of-art cryogenic electron microscopy (cryo-EM) can provide 3–5 Å resolution and has been extensively used to solve the structures of proteins. Cryo-EM has been used to identify the binding location of nanoparticles within proteins, but it could not identify explicitly which atoms or functional groups in the protein are bound to the nanoparticle [19].

X-ray crystallography, NMR, and MS are commonly used to determine the precise structure of organic compounds. X-ray crystallography is a powerful technique for determining the atomic structure of crystalline materials including small molecules, proteins, and ordered solids. However, its application in determining the structure of ligands on nanoparticles is more challenging and less common due to the complex and heterogeneous nature of nanomaterials. Nanoparticles with disordered or mixed ligand shells often fail to crystallize into high-quality crystals required for X-ray crystallography. While X-ray crystallography has been used to determine the structure of ligands on nanoparticles, its application is primarily limited to crystalline systems, ordered superlattices, or atomically precise nanoclusters. For instance, when nanoparticles and ligands form highly ordered superlattices or crystalline assemblies, X-ray crystallography can be used to determine ligand packing and orientation, providing insights into how ligands mediate interparticle interactions and stabilize the lattice [20,21]. Atomically precise nanoclusters, nanoparticles having diameters of <2 nm and well-defined structures, are particularly suitable for X-ray crystallography. When single crystals can be obtained, X-ray diffraction can determine the complete structure of atomically precise nanoclusters, including the core structure as well as the conformation and orientation of the ligand shell [22,23]. This level of precision is impossible to achieve for large heterogeneous nanomaterials.

NMR, the workhorse for structure determination of organic compounds, is highly useful for analyzing the structure and dynamics of ligands on nanomaterials [24,25]. Ligands bound to nanomaterials exhibit distinct spectral

features compared to the free ligand, including line broadening and peak shift. Line broadening is commonly observed for ligands on the nanomaterial surface, attributed to factors such as restricted motions in surface-bound ligands, heterogeneous chemical environment, and altered relaxation dynamics, which lead to decreased spin-spin relaxation time and increased dipolar relaxation. Nuclei closer to the nanoparticle surface show greater peak broadening than those further away. When the rotational restriction becomes more severe, it leads to significant line broadening, often causing the peak to appear as if it has disappeared. These can be seen in the studied by Murphy and coworkers who investigated the NMR spectra of 11-mercaptohexadecyl)trimethylammonium bromide (MTAB) conjugated to gold nanospheres (AuNS) of different sizes (Figure 1A) [26]. The peak at ~ 1.2 ppm, which corresponds to the main chain (mc) protons of MTAB, is broader than the peak of the head group (hg) protons at ~ 3.1 ppm, which are further away from AuNS surface (Figure 1B). Protons ω and ψ , the closest to AuNS, appear completely disappeared in MTAB-AuNS. Results in Figure 1B also show that the line broadening became more pronounced with increasing AuNS size. With regard to peak shift, ligands tethered to nanomaterial surfaces generally shift downfield, and several factors contribute to this. For interacting surfaces such as metals or semiconductors, electron density can be partially withdrawn from the ligand, deshielding nearby protons and causing a downfield shift. Additionally, these surfaces can create a paramagnetic or polarizable environment, altering the magnetic shielding of adjacent protons and further contributing to the downfield shift [27,28]. Protons near the nanoparticle surface may also interact with neighboring ligands, thus enhancing deshielding effects. Protons closest to the nanoparticle surface experience the strongest deshielding, resulting in the largest downfield shifts. In the example in Figure 1B, the hg protons shifted downfield from 2.99 ppm in the free MTAB to 3.05 ppm for 1.2 ± 0.3 nm AuNS. The results also showed that the downfield shift increased with increasing particle size, to 3.23 ppm for 10.8 ± 0.8 nm AuNS and then plateaued for larger AuNS (Figure 1C). Larger nanoparticles exhibit increased ability to alter electron density, reduced ligand mobility, and increased ligand-nanoparticle interactions due to larger surface area, all of which contribute to stronger deshielding and larger peak shifts.

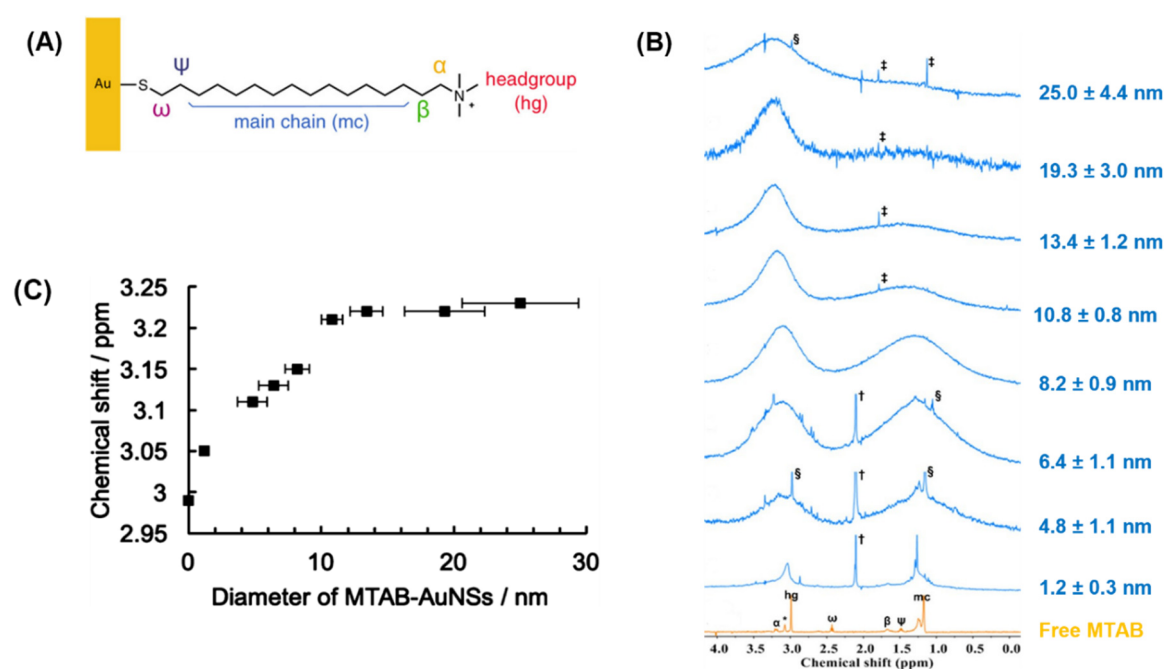


Figure 1. NMR analysis of ligand structure on gold nanospheres. (A) MTAB-functionalized AuNS. (B) ^1H NMR spectra of the free and AuNS-bound MTAB in D_2O , showing increased line broadening with increasing particle diameter. \ddagger : Residual acetone signal. \ddagger : Signals from impurities of plastic centrifugation tubes. \S : Residual MTAB signal. $*$: Signal from the headgroup protons in MTAB. (C) Chemical shift of hg headgroup protons in AuNS-bound MTAB vs. the diameter of AuNS, showing increased downfield shift with increasing particle size. Reprinted with permission [26]. Copyright 2019, American Chemical Society.

The results in Figure 1 demonstrate that NMR spectroscopy for ligand structure analysis becomes more challenging for larger nanoparticles due to significant line broadening. Additionally, NMR requires milligram scale materials in order to obtain measurable signals. For ligands on nanoparticles, the weight percent of the surface ligand decreases exponentially as the nanoparticle size increases [29]. As a result, a larger amount of nanomaterials

is required, which is challenging for nanomaterials having low solubility or are difficult to synthesize in large quantities. In contrast, nanoclusters with particle sizes smaller than 2 nm give a higher concentration of surface ligands, and as such, NMR has been extensively used in the structural analysis of nanoclusters to obtain precise ligand structure, particularly for atomically precise nanoclusters. In a remarkable work, Jin and coworkers employed ^1H NMR spectroscopy to determine the ligand structure, including the detailed bonding modes of the surface ligands, of a glutathione (SG)-capped atomically precise gold nanocluster, $\text{Au}_{25}(\text{SG})_{18}$ [30]. The ^1H NMR spectrum of $\text{Au}_{25}(\text{SG})_{18}$ revealed two distinct doublets (7 and 7', Figure 2B), which are assigned to the alpha protons of the thiolate ($-\text{CH}_2\text{S}$) in the ligand. The peak integration ratio was 2:1, indicating that the protons experience two different chemical environments. The integration ratio, 2:1, aligns with the proposed two-mode ligand structure on the Au_{25} core: Mode I with 12 ligands and Mode II with 6 ligands (Figure 2A). Furthermore, NMR revealed differences in the reactivity of the two ligand modes in $\text{Au}_{25}(\text{SG})_{18}$. Upon treating with an oxidizing reagent, $\text{Ce}(\text{SO}_4)_2$, Mode II peaks disappeared first before Mode I (Figure 2B), indicating higher stability of the Mode I than the Mode II ligands. When treated with a lower concentration of $\text{Ce}(\text{SO}_4)_2$, Mode I ligands remained unchanged even after 5 days, further supporting the higher stability of Mode I ligands.

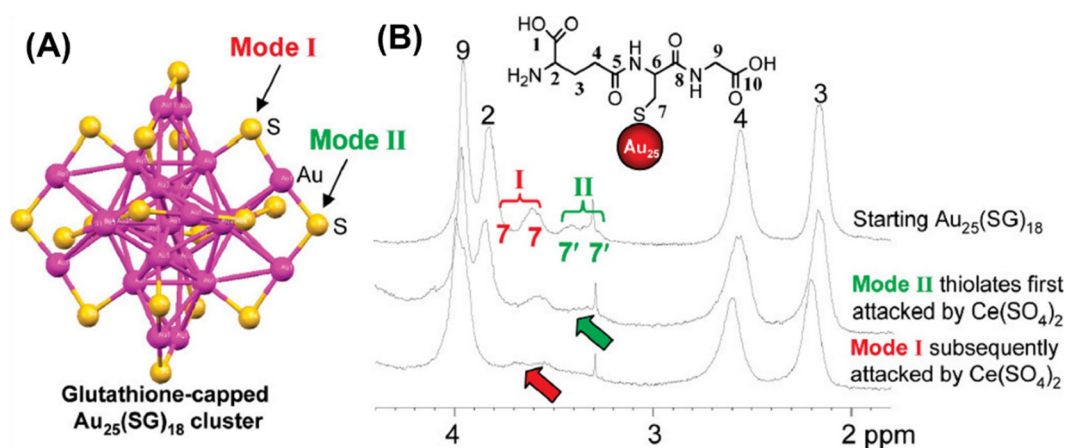


Figure 2. Determining ligand structure of $\text{Au}_{25}(\text{SG})_{18}$ nanocluster by NMR. (A) Structure of $\text{Au}_{25}(\text{SG})_{18}$. Only S of the ligand is shown for clarity. Au: purple; S: yellow. Each Mode I ligand coordinates to one inner and one outer Au, and each Mode II ligand coordinates to two outer Au. (B) ^1H NMR spectra of $\text{Au}_{25}(\text{SG})_{18}$ in D_2O before and after treating with $\text{Ce}(\text{SO}_4)_2$ over time. Oxidation affected Mode II ligands (7') first, and then Mode I ligands (7). Reproduced with permission [30]. Copyright 2009, American Chemical Society.

Mass spectrometry is a powerful technique for the characterization of chemical composition, molecular structure, and elemental distribution on nanomaterial surface. MS determines the structure and composition by analyzing the mass-to-charge ratio (m/z) of the fragments generated from the material. The accuracy of MS in surface analysis is governed by the type of the ionization method and the sensitivity of the mass analyzer [31]. Several MS techniques have been used to analyze nanomaterial surfaces. High-resolution electrospray ionization mass spectrometry (ESI-MS) is effective in determining the structure of small nanoclusters, offering high sensitivity and resolution for low molecular weight ligands [32]. For large nanoparticles and nanoparticles with more complex organic ligands, soft ionization techniques such as laser desorption/ionization (LDI) and matrix-assisted laser desorption/ionization (MALDI) are commonly used. For nanomaterials, however, the ionization efficiency of LDI or MALDI can be affected by the interaction of the ligand on the nanomaterial surface, which may hinder ligand release during analysis and lead to weak or undetectable signals. Also, ligands that bond strongly to nanomaterials may not be completely released, resulting in incomplete detection of surface species. Other challenges in using MS to characterize nanomaterial ligands include sample preparation, such as incomplete purification of nanoparticles or porous nanomaterials that may trap impurities, which can introduce artifacts and complicate data analysis.

Chiodo and coworker employed a Fourier transform ion cyclotron resonance (FTICR) mass spectrometer with high resolution and high mass accuracy to characterize complex surface ligand structures [33]. Using multiple MS techniques, including LDI-MS, MALDI-MS, MS/MS and FTICR combined with MALDI/LDI-MS (LDI/MALDI-FTICR MS), the authors characterized the ligand structure and the S-Au bond of a ~ 2 nm gold nanoparticle (AuNP). Figure 3 shows the mass spectra and analysis of ovalbumin peptide (OVA)-functionalized AuNPs. Using LDI-FTICR MS, a low intensity pseudomolecular ion, $[\text{M} + \text{Na}]^+$, was detected (Figure 3A), supporting the conjugation of the OVA ligand on AuNP. During the analysis by MALDI-FTICR MS, the authors

found that using 1,5-diaminonaphthalene (1,5-DAN) as the matrix improved the signal intensity by >80 times and enabled the detection of additional pseudomolecular ions such as $[M + Au]^+$ and $[M + 2 Au - H]^+$ (Figure 3B). The detection of these unique Au-bound species provides strong evidence for the presence of thiol-gold coordination on AuNP surface, which is impossible to characterize using other traditional analytical techniques like NMR. Further MS/MS analysis of Au-containing fragmentations (Figure 3C) suggested preferential binding site of Au^+ (Figure 3D).

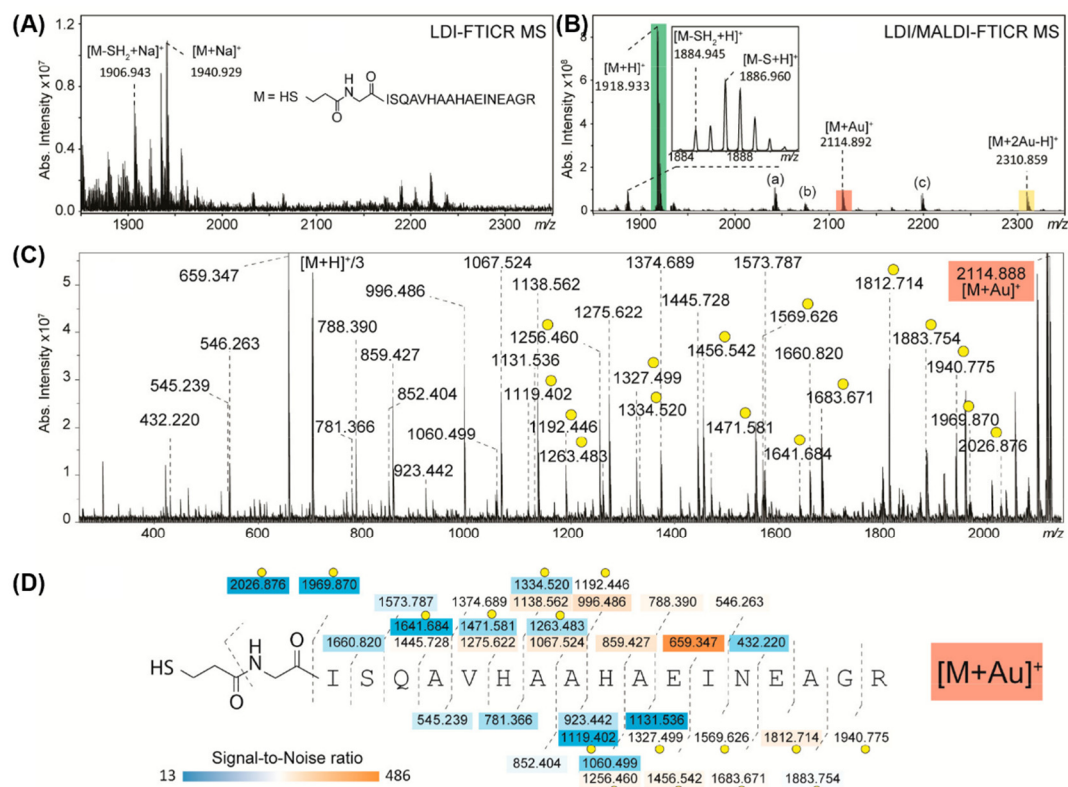


Figure 3. Ligand structure analysis of OVA-functionalized AuNPs by mass spectrometry. (A) LDI-FTICR MS spectrum, showing pseudomolecular ion $[M + Na]^+$. (B) LDI/MALDI-FTICR MS spectrum using 1,5-DAN matrix, showing additional pseudomolecular ions: $[M + H]^+$, $[M + Au]^+$ and $[M + 2 Au - H]^+$. (C) MS/MS spectrum of $[M + Au]^+$ showing detailed fragmentation. (D) Collision-induced dissociation (CID) analysis of the MS/MS spectrum in (C), showing sequence coverage and Au-coordinated fragment ions (highlighted with yellow circles). Reproduced with permission [33]. Copyright 2017, American Chemical Society.

3. Quantification of Ligand Density

Ligand density is defined as the quantity or mass of ligands per unit area of the nanomaterial surface or the unit mass of the nanomaterial, typically expressed as weight/mole/molecules per nm^2 or mg. The amount of ligands on nanomaterial can directly impact the physicochemical properties and the functions of nanomaterials [11]. Calculating ligand density requires two pieces of information: the quantity of ligands and the total surface area or weight of the nanomaterial. The total surface area of the nanomaterial is often estimated from the size and shape of the nanomaterial measured by microscopy techniques such as TEM. Direct measurement by techniques such as gas adsorption gives the total surface area, which includes not only the external surface area but also surface areas of accessible internal pores.

A number of methods have been used to quantify the ligand density on nanomaterial [25,34]. Thermogravimetric analysis (TGA) is widely used for quantifying ligand density on nanomaterials for its convenience and straightforward operation [35]. It measures the mass loss as the nanomaterial is heated, and the mass loss is directly correlated to the amount of ligand desorbed or decomposed from the nanomaterial. TGA is particularly well-suited for analyzing ligand density on nanomaterials having thermal decomposition behavior distinct from their surface ligands, such as organic ligands on metal or inorganic nanomaterials. However, the mass measured by TGA does not provide structural information of the surface ligands. Also, the technique is sensitive to impurities such as solvents, unbound ligands or organic contaminants, which can contribute to observed mass loss. Additionally, TGA requires milligrams of sample to give accurate measurements, which can be difficult to

obtain for certain nanomaterials. Despite these limitations, TGA is valuable for quantifying ligand density, especially when used together with other techniques to provide a more comprehensive understanding of nanomaterial surfaces. Below, we discuss structure-specific methods for the quantification of ligand densities on nanomaterials, including traditional analytical techniques such as quantitative NMR (qNMR) and UV-vis spectroscopy, chemical assays, as well as emerging techniques that offer spatial resolution on single nanoparticles or measure functional ligands available for receptor binding.

The qNMR spectroscopy is specifically developed for quantitative measurements [36]. By using a reference compound with known concentration as the calibration, qNMR can accurately determine the concentration of a sample. When applied to nanomaterials, qNMR can quantify organic ligands with high specificity when the sample and preparation requirements can be met. Since NMR requires milligram-scale quantity of samples, sufficiently high ligand concentrations are needed in order to obtain reliable results. Additionally, sufficient solubility is required to ensure proper dispersion of nanomaterials in the NMR solvent. For larger nanoparticles having low ligand concentrations and displaying greater line broadening, qNMR experiments can become more difficult. A possible solution is to cleave the ligands from the nanoparticles prior to qNMR analysis, provided that the protocol does not degrade the ligands or introduce additional impurities.

On the other hand, if the ligands contain F or P which are absent in the nanomaterial itself, ^{19}F qNMR or ^{31}P qNMR can be used without having to go through complicated sample separation. We applied ^{19}F qNMR to determine the ligand density on large nanoparticles, 87 ± 8.0 nm diameter silica nanoparticles (SNPs) [37]. ^{19}F is a 100% naturally abundant nuclei and ^{19}F NMR has comparable sensitivity ($\sim 88\%$) to ^1H NMR. The ligands, D-mannose (Man) and D-galactose (Gal), were conjugated on SNPs via azide-alkyne click reaction using perfluorophenyl azide (PFPA, Figure 4A). As the F atoms are present only in PFPA and not in SNPs, using ^{19}F qNMR simplifies the quantification process as no complex separation is needed. The samples can be directly subjected to ^{19}F qNMR without background interference from SNPs. The ligand density obtained from ^{19}F qNMR, 6.4 ± 0.2 nmol/nm 2 for Man-SNP, was also compared with the results from TGA (13.0 ± 3.4 nmol/nm 2). The higher values measured by TGA could be from trapped solvents and other organic impurities in the nanoparticles.

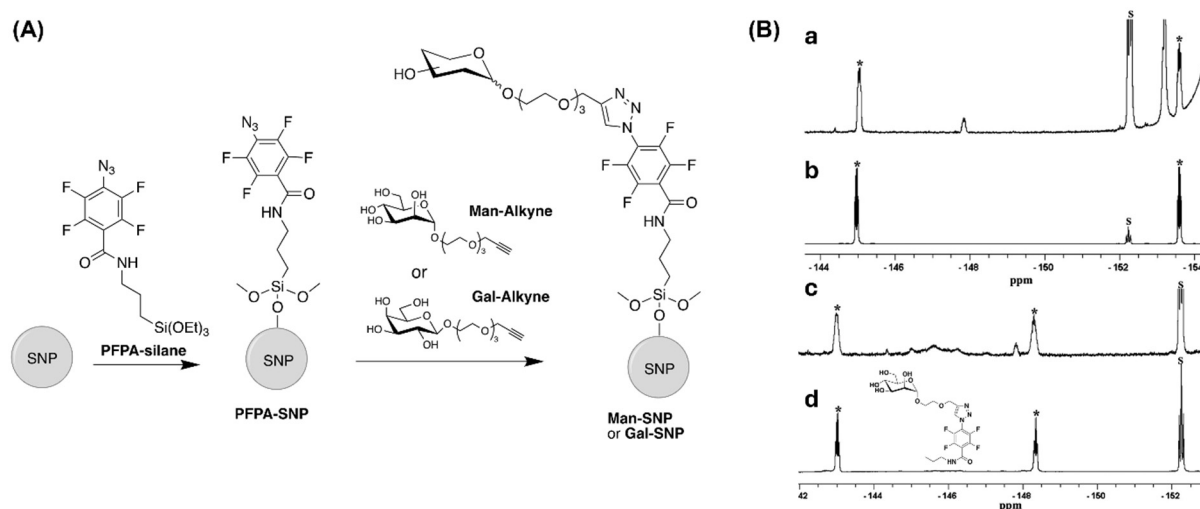


Figure 4. Determining ligand density on nanoparticles by ^{19}F qNMR. (A) Conjugation of Man or Gal to SNPs via PFPA-click reaction. (B) ^{19}F NMR spectra of (a) PFPA-SNP after treating with HF, (b) PFPA-silane, (c) Man-SNP after treating with HF, (d) a model compound. Nanoparticle samples were treated with 5% HF for 1 h, lyophilized in the presence of an in-line trap with CaO, and the residual was dissolved in methanol with methyl pentafluorobenzoate as the internal standard. Marked as “*” are F-2,6 and F-3,5 in the tetrafluorophenyl group, and “S” are from the methyl pentafluorobenzoate standard. Reproduced with permission [37]. Copyright 2015, American Chemical Society.

When multiple ligands are present on a nanomaterial, accurate quantification of each surface ligand can be challenging. Pérez-García et al. employed UV-vis spectroscopy combined with spectral deconvolution to quantify the densities of mixed ligands on AuNPs [38]. The sample was prepared via ligand exchange reactions from citrate-capped AuNPs, first with thiol-PEG-COOH and then with cytochrome C (Cyt C) and zinc porphyrin (Zn Porph) to give AuNP-PEG-Cyt C/Zn Porph (Figure 5A). The UV-vis spectrum of AuNP-PEG-Cyt C/Zn Porph showed overlapping peaks from Cyt C and Zn Porph, making it impossible to identify each ligand for quantification. To overcome this, the authors used CASA-XPS software and the Levenberg–Marquardt algorithm to deconvolute the

absorption spectra. Using this approach, the authors were able to identify bound Zn Porph and Cyt C and unbound Zn Porph (Figure 5B), from which the concentration of each bound as well as unbound ligand were determined. For ~20 nm AuNPs, the concentrations of conjugated Cyt C and Zn Porph were 0.42 μM and 1.3 μM , respectively, corresponding to 346 Cyt C and 1073 Zn Porph molecules per nanoparticle. For ~50 nm AuNPs, higher ligand densities were obtained, with the concentrations of Cyt C and Zn Porph at 0.11 mM and 1.3 mM, corresponding to 23,259 Cyt C and 35,168 Zn Porph molecules per nanoparticle.

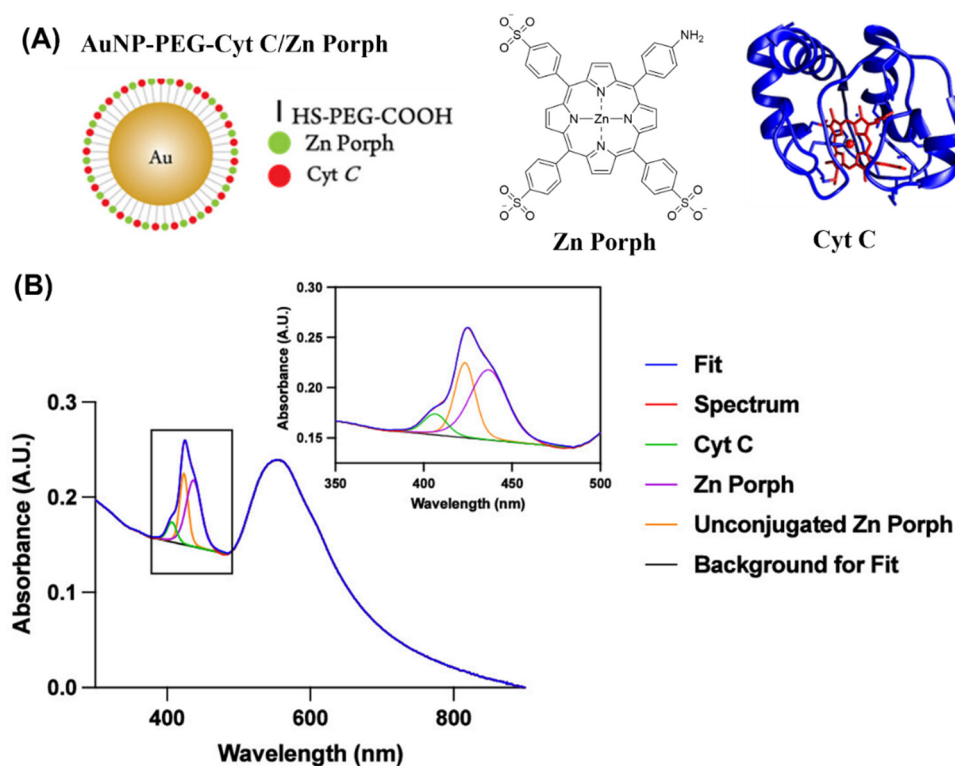


Figure 5. Quantification of mixed ligands using UV-vis spectroscopy combined with spectral deconvolution. (A) AuNPs functionalized with Zn Porph and Cyt C. (B) Deconvolution of Soret band in the UV-vis spectrum of AuNP-PEG-Cyt C/Zn Porph identified bound Zn Porph and Cyt C and unbound Zn Porph. Reproduced with permission [38]. Copyright 2023, American Chemical Society.

Surface-sensitive MS techniques, such as time-of-flight secondary ion mass spectrometry (ToF-SIMS), has also been used to quantify ligand density on nanoparticles [39]. ToF-SIMS utilizes a primary ion beam (e.g., Bi^+ , Ga^+ , C_{60}^+) to bombard a sample, ejecting secondary ions from ligands or ligand fragments within the top 5–10 nm surface layer of the sample. While ToF-SIMS is traditionally applied to flat surfaces due to potential topographical effects, recent advancement has enabled the analysis of surface ligands on individual nanoparticles. For instance, Schweikert and coworkers used Au_{400}^{4+} clusters as projectiles to determine ligand density on DNA-functionalized anisotropic gold nanostars and isotropic gold nanospheres of comparable surface areas but different morphologies [40]. The Au_{400}^{4+} clusters produced abundant secondary ions, with each impact probing a 10–15 nm diameter area, giving sampling density of $2\text{--}4 \times 10^6$ projectiles across a 125 μm radius area to ensure statistically robust data collection. Results showed higher DNA density on gold nanostars than on gold nanospheres. Furthermore, nanostars with ~3 branches per particle had the highest DNA density whereas nanostars with more branches showed reduced DNA loading, likely due to steric hindrance at branch-core junctions.

Chemical assays, when specific to certain ligand types, can be a powerful method for the quantification of ligand density. The anthrone-sulfuric acid or phenol-sulfuric acid assays, for example, is highly specific for carbohydrates. It works by converting carbohydrates into furfural derivatives under acidic conditions, which then react with anthrone to form a blue-green complex ($I_{\text{max}} = 620 \text{ nm}$) (Figure 6A) [29], or with phenol to form a yellow-orange complex ($I_{\text{max}} = 490 \text{ nm}$) [41]. The assay has been employed to quantify carbohydrate density on nanoparticles. In the example shown in Figure 6B, we conjugated carbohydrates to AuNPs via a photoconjugation reaction using PFPA, and determined the ligand density by treating carbohydrate-capped AuNPs with anthrone/sulfuric acid and comparing the absorption to a standard calibration [42]. By comparing the amount of Man conjugated on AuNPs with the amount of Man initially added, the photoconjugation yield can be calculated. Results showed decent coupling yields for all samples tested (53–85%, Figure 6C), demonstrating high efficiency

of the photoconjugation reaction. Even at low ligand concentrations, high yields were achieved (78–85%), although the overall surface coverage was low (0.11–1.1%) due to low amount of Man initially added (0.1–1 nmol/mg).

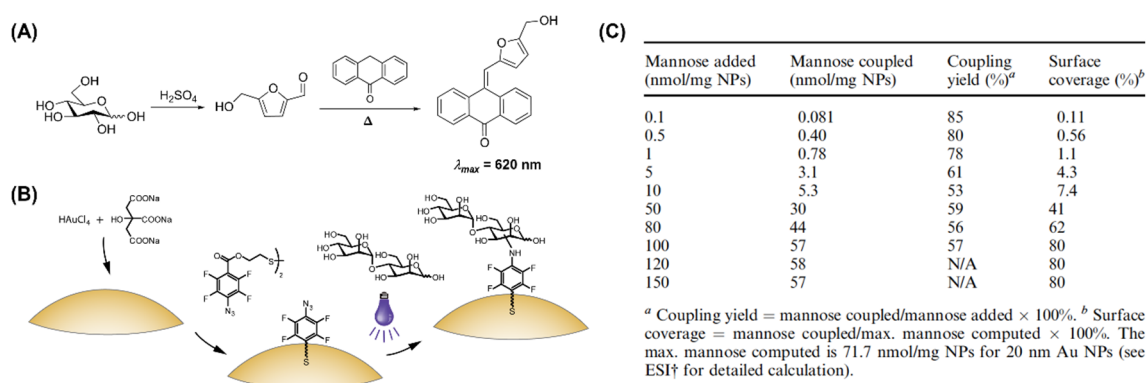


Figure 6. Anthrone-sulfuric acid assay to quantify carbohydrate ligands on nanoparticles. (A) Reaction of D-glucose with sulfuric acid followed by anthrone to give a colored anthracenone product. (B) Photochemical conjugation of carbohydrates on AuNPs. (C) Ligand density, conjugation yield, and surface coverage of Man-AuNPs. Reproduced with permission [42]. Copyright 2009, Royal Society of Chemistry.

Nanomaterials often have heterogeneous surfaces with varying crystalline facets, defects, and curvature, which can lead to non-uniform ligand attachment [14,15]. Heterogeneity in nanoparticle size, shape, surface morphology, and ligand distribution can also cause variations in ligand density both among and within individual nanoparticles. In addition, factors such as ligand presentation and ligand-ligand interactions through functional groups and/or spacer linker further contribute to this variation. The ability to map ligand density with high spatial resolution is thus important for understanding the ligand attachment patterns, distribution, and reactivity across nanomaterial surface. The common quantification methods discussed above give the global average and cannot resolve particle-to-particle variations in ligand density. Below, we discuss two examples that used emerging microscopy techniques to achieve single particle analysis and high spatial resolution.

Huang et al. exploited electron energy loss spectroscopy (EELS) combined with aberration-corrected dark-field scanning transmission electron microscopy (ADF-STEM) to quantify and image ligand density on cetyltrimethylammonium bromide (CTAB)- or MTAB-capped gold nanorods (AuNRs) at sub-nanometer spatial resolution [43]. Samples were prepared by depositing AuNRs on single-layer graphene grids to reduce background noise and enhance detection sensitivity. Following baking the samples in vacuum at 130 °C, EELS maps were generated by integrating the signals and dividing them by the nanorod surface area (Figure 7). The authors found that the ligand density was anisotropic on CTAB-AuNR, with lower ligand coverage at the nanorod ends at 0.88 ± 0.4 molecules/nm² compared to the nanorod sides at 1.03 ± 0.4 molecules/nm². On the other hand, the ligand density was more uniform across the surface of MTAB-AuNR, with 1.04 ± 0.2 molecules/nm² at the ends and 0.97 ± 0.2 molecules/nm² at the sides.

Yan and coworkers employed nanoflow cytometry (nFCM) to quantify ligand density on liposomes at the single-particle level, achieving high throughput with analysis of up to 10,000 liposomes per minute (Figure 8) [44]. For ligand density determination, the authors used fluorescently labeled recombinant receptors as probes that bind specifically to ligands on liposomes. nFCM simultaneously measured side-scattering for particle size and fluorescence for ligand quantification. Using this method, the authors identified optimal ligand density for effective cell targeting: 0.5–2.0 ligands/100 nm² for folate, 0.7 ligands/100 nm² for transferrin, and (0.2 ligands/100 nm²) for HER2 antibody. Note that this method only detects ligands available for receptor binding, not the total ligand density. Ligands having undesired orientation, shielded by PEG, and denatured or overcrowded ligands were not detected.

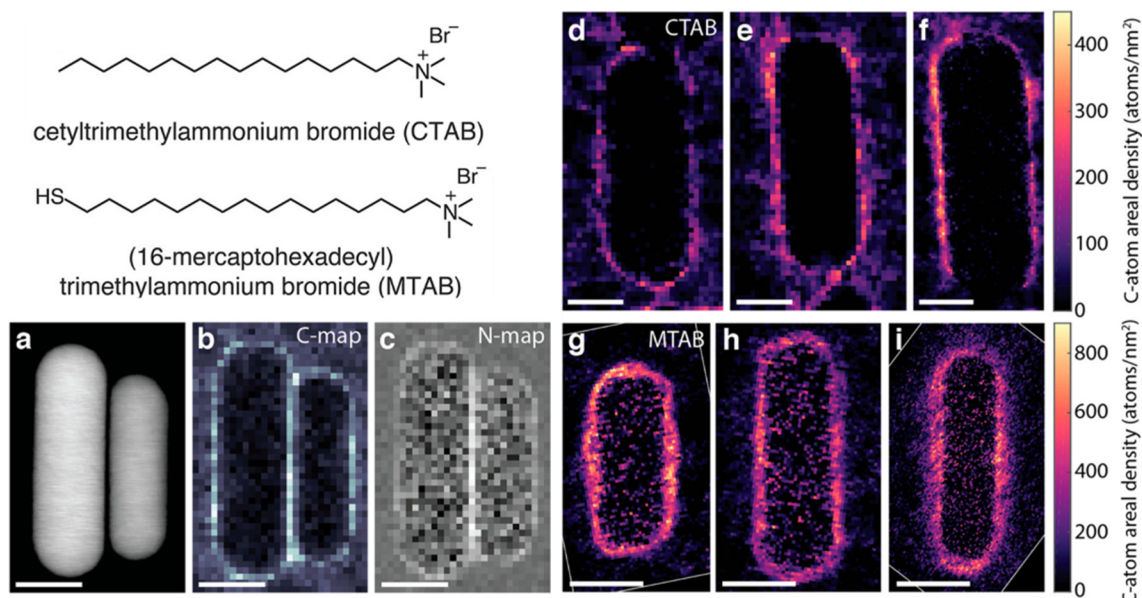


Figure 7. Mapping ligand density on CTAB-AuNR and MTAB-AuNR using ADF-STEM and EELS. (a) ADF-STEM image of CTAB-AuNRs. (b) Carbon and (c) nitrogen EELS maps of the two CTAB-AuNRs in (a). (d–i) EELS carbon density maps of (d–f) CTAB-AuNRs and (g–i) MTAB-AuNRs. The atomic areal intensity is the 2D projected areal density of C atoms after subtracting the graphene background. Scale bars are 15 nm in (a–c), and 10 nm in (d–i). Reproduced with permission [43]. Copyright 2019, American Chemical Society.

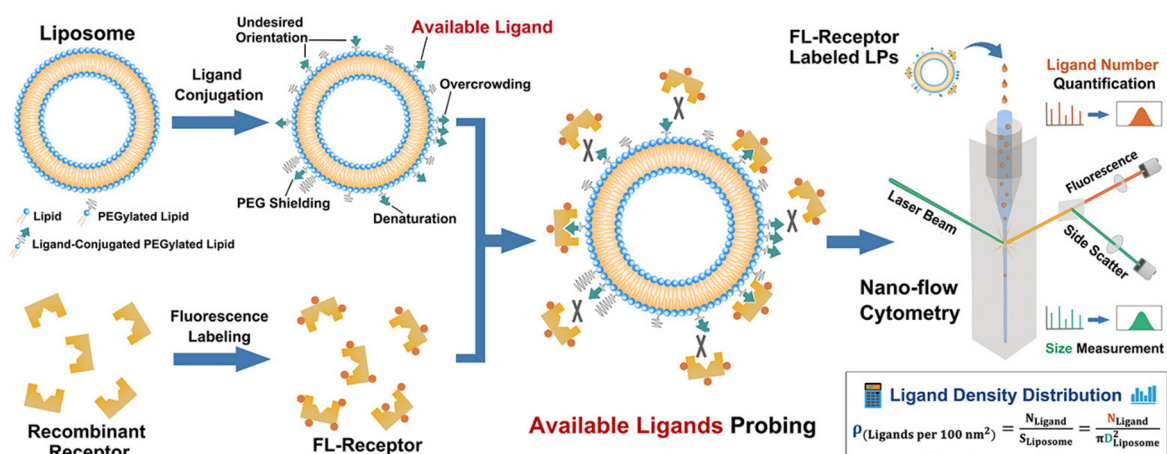


Figure 8. Quantification of ligand density on single liposomes: Sample preparation and quantification of available ligands by nFCM. Reproduced with permission [44]. Copyright 2022, American Chemical Society.

4. Quantification of Surface Functional Groups

A number of analytical techniques have been employed and developed to quantify functional groups on nanomaterials [45–47]. Titration methods, qNMR, MS, and various spectroscopy methods are used to quantify total functional groups on nanomaterials. Quantification using these methods focuses on detecting the intrinsic chemical properties of functional groups or elements in the nanomaterial, eliminating the need for external labels or probes. On the other hand, probe-based methods use chromophore-based probes or cleavable probes that interact or react with functional groups on the nanomaterial to produce measurable changes in absorbance or emission. Quantification is achieved by comparing the measured signals to a standard calibration curve. Probe-based methods measure functional groups that are accessible to the probe molecules, referred to as derivatizable functional groups. As such, differences in the relative size, steric hindrance, and reactivity contribute to inaccuracies in these methods.

Table 1 summarizes the working principle, type and quantifiable functional groups of various methods that have been used to quantify functional groups on nanomaterials. Readers are referred to a recent review on this topic by Resch-Genger and coworkers for comprehensive discussions of the techniques and examples [45]. Each method offers its own advantages, limitations, and contexts of application, and multiple complementary techniques

are often necessary to gain a comprehensive characterization. Here, we discuss cleavable probes and give an example where the total and derivatizable functional groups were measured using different probes and quantification techniques.

Table 1. Working principle, type and quantifiable functional groups (FGs) of methods for quantification of functional groups on nanomaterials.

Method	Working Principle	Type of FGs	Total vs. Derivatizable FGs	Examples of Quantifiable FGs
Potentiometric Titration	Measures electrochemical potential changes; determines equivalence points for (de)protonable groups.	(De)protonable groups	Total	-COOH, -NH ₂ , -SH
Conductometric Titration	Measures conductivity changes during acid/base titration.	Charged groups	Total	-COOH, -NH ₂
Boehm Titration	Neutralizes acidic FGs on carbon materials; calculates density from back titration of unreacted FGs.	Acidic oxygen-containing FGs	Total	-COOH, phenols, lactonic groups
Optical Assays	Dye-based reporters interact or react with FGs, yielding measurable absorption/emission signals.	Dye interacting or reactive FGs	Derivatizable; limited by dye size and steric effects	-NH ₂ , -SH, -CHO, -N ₃
Cleavable Probes	Reporter molecules react with FGs, which is then cleaved, and quantified using photometric or fluorometric assays.	Dye reactive FGs	Derivatizable; limited by dye size and steric effects	-NH ₂ , -COOH, -CHO
Adsorption/Desorption Assays	Reporter molecules electrostatically interact with surface FGs; desorbed reporters are quantified.	Reporter interacting FGs	Accessible FGs; Relies on stoichiometry factor calibration	Charged groups: -COOH, -NH ₂ , sulfates
NMR Spectroscopy	Analyzes chemical shifts of nuclei; high chemical specificity.	FGs containing NMR active nuclei; distinguishes surface-bound and free species.	Total	H-, C-, N-, F-, P-containing FGs
Inductively Coupled Plasma (ICP)-MS/ICP-OES (Optical Emission Spectroscopy)	Measures elemental concentrations to infer FG or ligand counts, often labeled with detectable elements, high sensitivity	Most FGs, except those containing only light elements of H, C, N, O, F	Total or derivativizable	S- and P-containing FGs, metal-complexing FGs
Vibrational Spectroscopy	Measures molecular vibrations corresponding to specific FGs, e.g., IR and Raman, including surface-enhanced variants for increased sensitivity.	FGs with strong dipoles (IR), or containing bonds with high polarizability (Raman)	Total	-COOH, -NH ₂ , -SH, -OH, -SiOH, -CHO, C-C, S-S, etc.

Cleavable probes typically consist of three parts: a reactive group that binds to or reacts with the functional group, a cleavable linker that facilitates the release of the reporter, and a reporter molecule for detection [48,49]. The linker is designed with cleavable covalent bonds such as disulfide, pH sensitive hydrazone or protecting groups such as fluorenylmethoxycarbonyl (Fmoc) which is a base-labile protecting group for amines. Upon cleavage, the reporter molecule is released, and the functional group is quantified by measuring the concentration of the released reporter. An advantage of using cleavable probes is that the indirect quantification of the cleaved reporter improves accuracy by eliminating errors caused by light scattering, which can occur in the direct measurements on nanoparticles.

Johnston and coworkers employed several methods to quantify the density of amino groups on silica nanoparticles, including using a dye-based reporter, a cleavable probe, and qNMR [50]. For the dye-based reporter

method, the amine-functionalized silica nanoparticles were allowed to react with ninhydrin to produce a colored product, Ruhemann's purple (Figure 9A). The density of surface amino groups was quantified by measuring the concentration of Ruhemann's purple ($I_{max} = 570$ nm) using UV-vis spectroscopy, giving 47–320 $\mu\text{mol g}^{-1}$ depending on the nanoparticle size and surface coverage. In the cleavable probe approach, the amine on the nanoparticle first reacted with 4-nitrobenzaldehyde (4-NBA) to form an imine, which was then hydrolyzed to regenerate 4-NBA ($I_{max} = 275$ nm) for quantification by UV-vis spectroscopy (Figure 9B). This method resulted in higher amine density, 53–459 $\mu\text{mol g}^{-1}$ (Figure 9D), than the dye-based reporter method, hypothesized as reduced steric hindrance of 4-NBA compared to ninhydrin. In the third method, amines were labeled with a fluorinated probe, trifluoromethylated benzaldehyde, via a reaction between the amine and the aldehyde to form an imine product (Figure 9C). Quantification using solid-state ^{19}F NMR gave amine density of 40–380 $\mu\text{mol g}^{-1}$, which is similar to the results obtained from the 4-NBA assay (Figure 9D). Finally, the amine was quantified by dissolving silica nanoparticles in a solution of 0.4 M NaOD in D_2O at 45 °C for 3 h and analyzing by ^1H qNMR using maleic acid as the internal standard. The result, 57–655 $\mu\text{mol g}^{-1}$, is the highest of all methods as ^1H qNMR measures the total amines. On the other hand, the probe-based methods in Figures 9A–9C only measure amines accessible to the probes. The larger size of the probes compared to the amine means that not all amines are able to react with the probes in a 1:1 stoichiometry. This leads to lower measured concentrations than that obtained by ^1H qNMR. In fact, the largest probe, ninhydrin, generally gave the lowest result (Figure 9D).

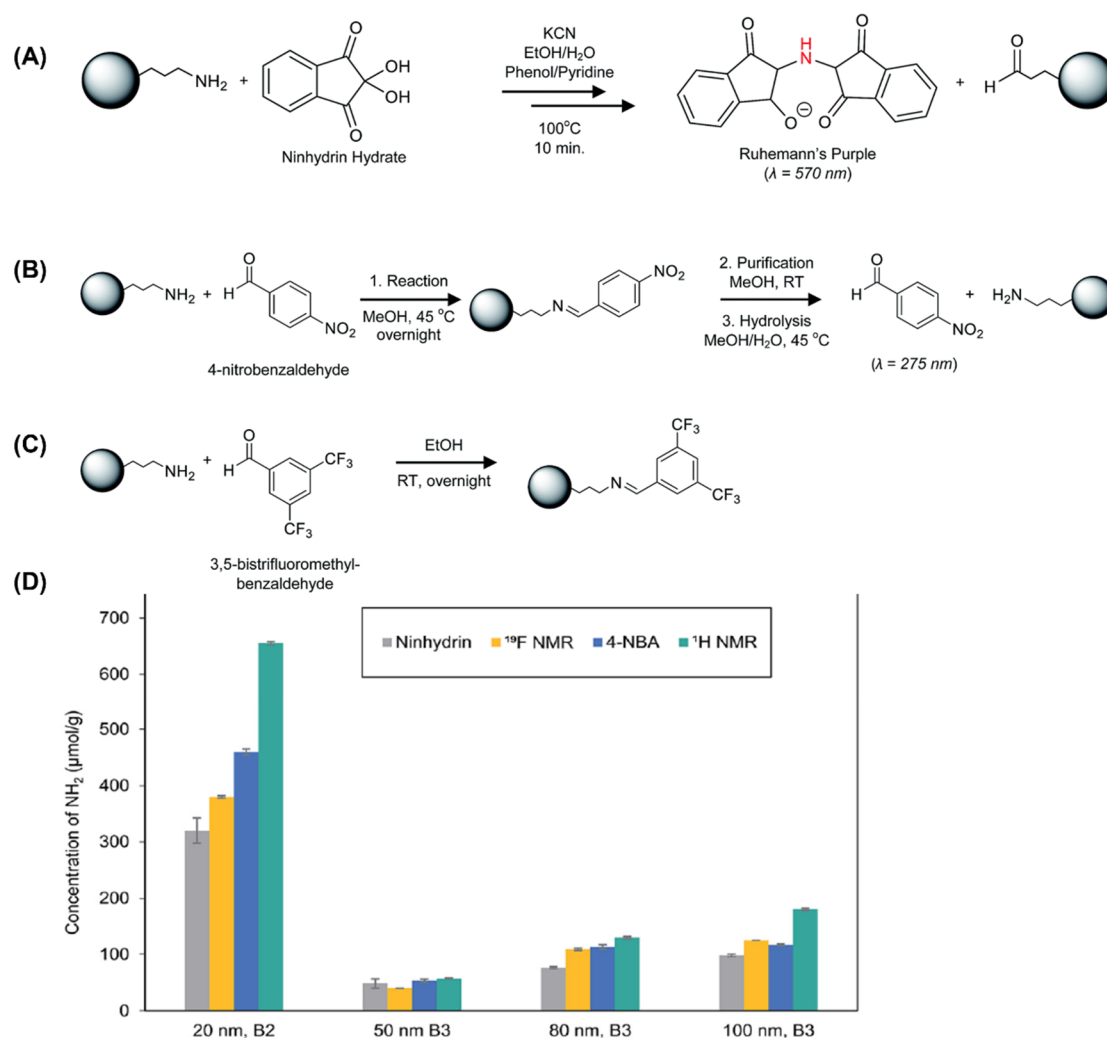


Figure 9. Probe-based methods for the quantification of amine density on silica nanoparticles. (A) Dye-based reporter method using ninhydrin to give Ruhemann's purple for quantification by UV-vis spectroscopy. (B) Cleavable probe method using 4-NBA and UV-vis spectroscopy. (C) Quantification by ^{19}F NMR using an F-containing reporter, trifluoromethylated benzaldehyde. (D) Comparison of amine density determined by methods (A–C) and ^1H qNMR. Reproduced with permission [50]. Copyright 2019, Royal Society of Chemistry.

5. Quantification of Surface Reactions

Quantitative analysis of reactions on nanomaterial surfaces is necessary for both fundamental understanding of the surface reaction and for optimizing nanomaterial properties and performance [51,52]. Like any chemical reactions, quantitative analysis of reactions on nanomaterial surfaces provides insights into reaction stoichiometry, kinetics, thermodynamics, and yield, enabling the identification of active sites and mechanisms unique to nanomaterials. Quantitative analysis also provides means to compare across nanomaterials under identical reaction conditions, ensuring batch-to-batch reproducibility and scalability of nanomaterials for commercial applications. Surface reactions are generally carried out by way of direct functionalization of nanomaterials, ligand exchange, or through conjugation reactions with complementary functional groups [53].

NMR is again a powerful tool to determine the product structure of surface reactions, particularly for small nanomaterials like nanoclusters. In the example shown in Figure 10, we carried out a ligand exchange reaction on $[\text{Au}_{11}(\text{PPh}_3)_8\text{Cl}_2]\text{Cl}$ (TPP: triphenylphosphine) using triphenylphosphine monosulfonate (TPPMS) as the incoming ligand [54]. $[\text{Au}_{11}(\text{PPh}_3)_8\text{Cl}_2]\text{Cl}$ undergoes nuclearity conversion to give $[\text{Au}_9(\text{TPPMS})_8]\text{Cl}_3$ as confirmed by high-resolution ESI-MS (Figure 10A). Characterizations of the product using a combination of NMR techniques, including ^1H , ^{31}P , 2D COSY (correlation spectroscopy) and 2D DOSY (diffusion-ordered spectroscopy), collectively confirmed the product structure. The results also revealed the purity of the product, with no evidence of free ligands or other impurities (Figure 10C).

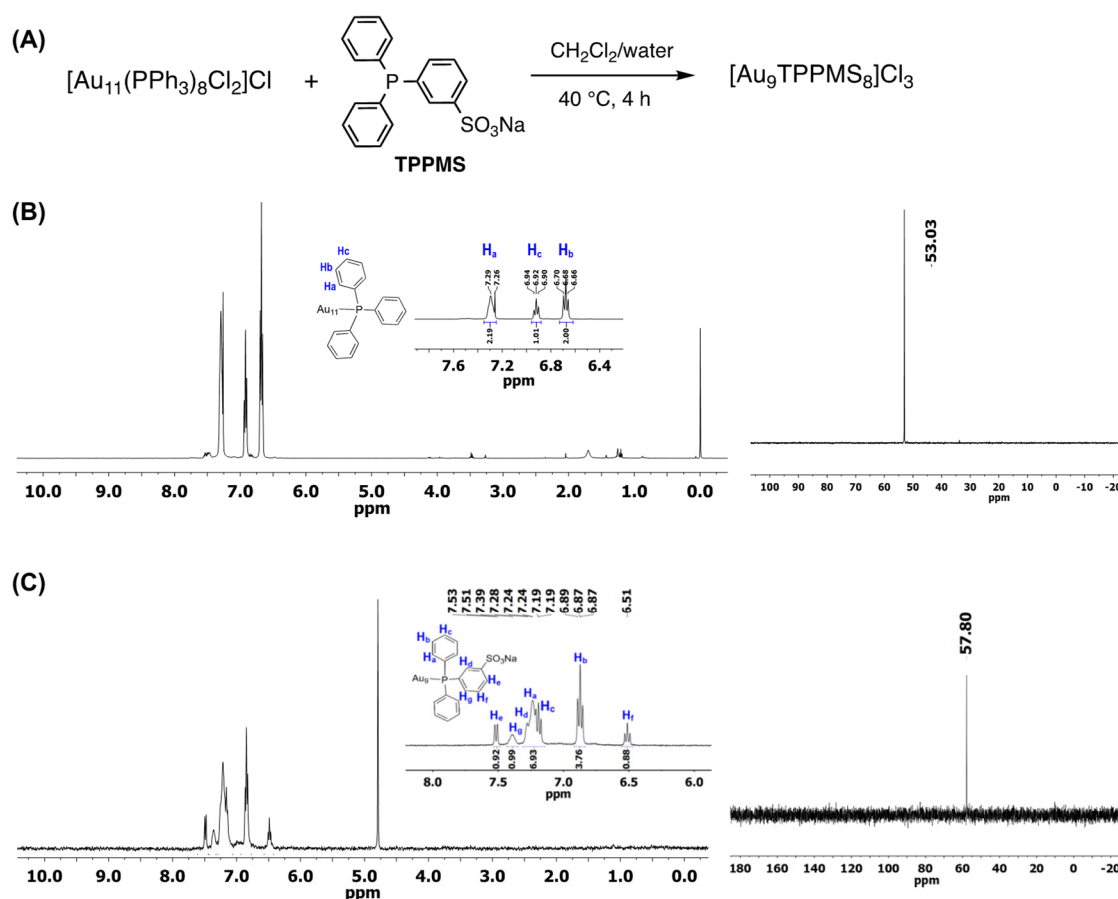


Figure 10. Studying surface reaction by NMR. (A) The ligand exchange reaction of $[\text{Au}_{11}(\text{PPh}_3)_8\text{Cl}_2]\text{Cl}$ with TPPMS to give $[\text{Au}_9(\text{TPPMS})_8]\text{Cl}_3$. (B) ^1H and ^{31}P NMR spectra of starting material $[\text{Au}_{11}(\text{PPh}_3)_8\text{Cl}_2]\text{Cl}$ in CDCl_3 . (C) ^1H and ^{31}P NMR spectra of product $[\text{Au}_9(\text{TPPMS})_8]\text{Cl}_3$ in D_2O (0.6 mM). Peak assignments were confirmed by 2D COSY NMR. Reproduced with permission [54]. Copyright 2021, Royal Society of Chemistry.

Epple and coworkers used qNMR and other spectroscopy techniques to quantify surface reactions on AuNPs [55]. The authors first converted the amino groups on glutathione (GSH)-capped AuNPs (~2 nm) to azide via a copper-catalyzed N_2 transfer reaction (Figure 11A). Subsequent click reaction of N_3 -AuNP with alkyne-functionalized dyes (FAM-alkyne and AlexaFluor-647-alkyne) gave FAM-AuNP and AlexaFluor-647-AuNP (Figure 11B). The number of surface ligands was determined using atomic absorption spectroscopy (AAS) and qNMR. AAS measurements gave the molar concentration of AuNPs. The ^1H qNMR analysis of GS-AuNP,

calibrated with maleic acid, gave ~125 GSH molecules per nanoparticle. After azidation, 118 GSH were converted to azido groups, giving a 94% reaction yield (Figure 11C). By measuring the concentration of dye molecules by UV-vis spectroscopy and the concentration of nanoparticles by AAS, the click reaction yield was calculated as 13% for FAM-AuNP (~6 FAM molecules/nanoparticle) and 23% for AlexaFluor-647-AuNP (~11 AlexaFluor-647 molecules/nanoparticle), respectively. The low yields were attributed to steric hindrance due to the large dye molecules and electrostatic interactions between dye molecules on the nanoparticle surface.

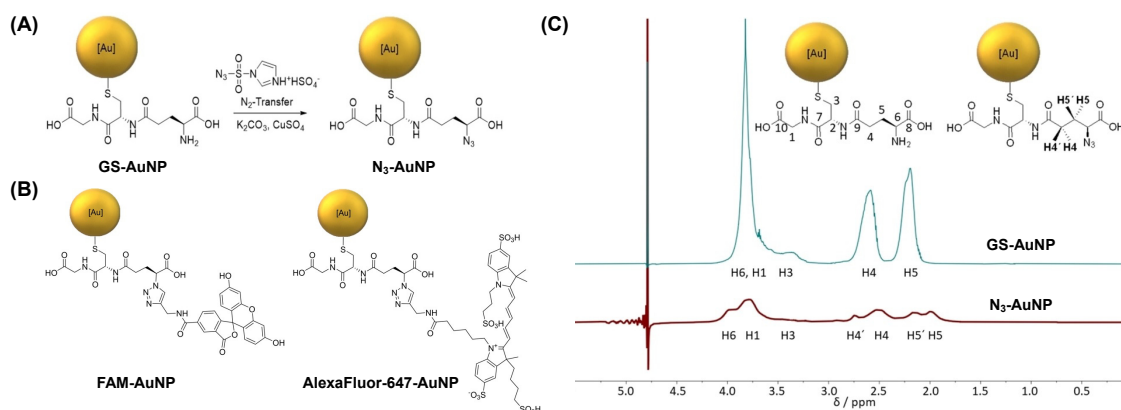


Figure 11. Determining the yield of surface reactions on nanoparticles by qNMR. (A) Azidation of GS-AuNPs to give N₃-AuNP. (B) FAM-AuNP and AlexaFluor-647-AuNP. (C) ¹H NMR spectra of GS-AuNP and N₃-AuNP, in 90% H₂O/10% D₂O at pH 8 with water suppression. Reproduced with permission [55]. Copyright 2021, Wiley.

We employed Raman spectroscopy to determine the kinetics of the Diels-Alder reactions on graphene supported on different substrates [56,57]. Monolayer pristine graphene has a characteristic Raman G band at ~1580 cm⁻¹. When the *sp*² carbons in graphene are converted to *sp*³ carbons after chemical functionalization, the D band at ~1350 cm⁻¹ appears in its Raman spectrum. At low degree of functionalization, the intensity ratio of the Raman D and G bands, *I*_D/*I*_G, serves as an indicator of the extent of functionalization (Figure 12A). To quantify reaction kinetics, a pseudo-first-order kinetic model was applied. Plotting $-\ln [1 - 0.067 \frac{I_D}{I_G}]$ against time yielded linear fits (Figure 12B), from which the rate constants were obtained. Results of the reaction between maleic anhydride (MAH) and graphene showed that Ni-supported graphene had the highest rate, 1.8–2.4 times higher than graphene supported on silicon wafer (SiO₂/Si, Figure 12C).

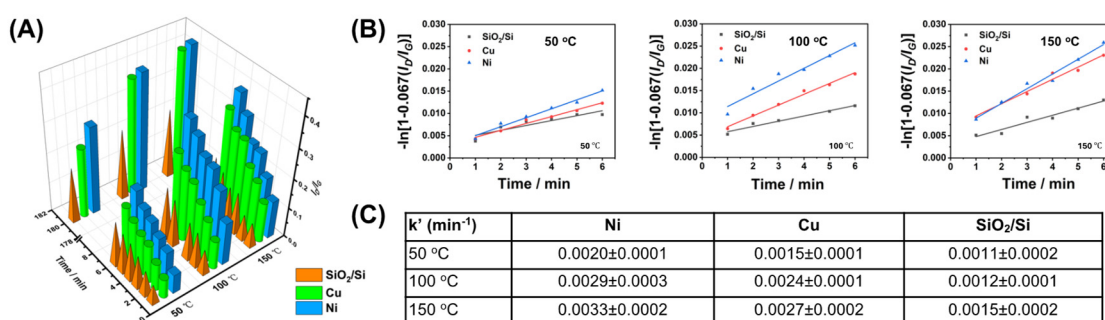


Figure 12. Determining rate constant of reactions on graphene by Raman spectroscopy. (A) *I*_D/*I*_G vs. reaction time and temperature for graphene supported on Ni, Cu or silicon wafer. (B) $-\ln [1 - 0.067 \frac{I_D}{I_G}]$ vs. time, and (C) the apparent rate constant *k'* (min⁻¹) for reaction of MAH with graphene supported on Ni, Cu or silicon wafer at 50 °C, 100 °C, and 150 °C. Reproduced with permission [56]. Copyright 2022, Royal Society of Chemistry.

Alivisatos and coworkers employed a combination of isothermal titration calorimetry (ITC), ¹H qNMR spectroscopy, X-ray diffraction, and modified Ising model to study the ligand exchange of myristate- or stearate-capped indium phosphide (InP) quantum dots (QDs) by zinc chloride [58]. The ligand exchange involves breaking van der Waals interactions between aliphatic chains of the ligands and forming new bonds with Zn²⁺. ITC results support the proposed mechanism, showing that ligand exchange reactions became more endothermic with increasing QD size and longer ligand chains. ¹H qNMR with mesitylene as the internal standard was used to track the ligand density before and after ligand exchange. Stearate-capped QDs generally have lower ligand densities

than myristate-capped QDs of similar sizes, at 1.9 ± 0.5 – 3.7 ± 0.9 ligands/nm² and 2.7 ± 0.7 – 5.1 ± 1.0 ligands/nm², respectively. For both ligand types, smaller QDs (e.g., 2.7 nm) gave higher ligand densities compared to larger QDs (e.g., 3.4 nm). After the ligand exchange, the ligand coverage decreased more for myristate-capped QDs to a normalized coverage of ~ 0.2 – 0.4 of the original density than for stearate-capped QDs, which decreased to ~ 0.3 – 0.5 of the initial density.

A recent work by Choi and coworkers quantified interparticle ligand exchange kinetics of thiol ligands on AuNPs using the technique of time-resolved small-angle neutron scattering (TR-SANS) [59]. Hydrogenated (hDDT) and deuterated dodecanethiol (dDDT) were used to functionalize AuNPs, which provide neutron contrast. Changes in scattering intensity over time were monitored at different temperatures to detect ligand exchange, and the normalized relaxation function, $R(t)$, was calculated to quantify the extent of ligand exchange. Further, an exponential decay model was applied to estimate exchange kinetics and rate constants. Results showed that at 25 °C, there was minimal ligand exchange even after 40 h. The ligand exchange was 11%, 34%, and 74% at 50, 60, and 70 °C, respectively after 40 h, and reached $\sim 100\%$ at 80 °C within 20 h (Figure 13A). First-order kinetic was observed, indicating that the ligand desorption was the rate-determining step (Figure 13B). The rate of ligand exchange increased with temperature, ranging from $3.4 \times 10^{-5} \text{ min}^{-1}$ at 50 °C to $1.6 \times 10^{-3} \text{ min}^{-1}$ at 80 °C. Arrhenius analysis yielded an activation energy of 29.1 kcal/mol (Figure 13C).

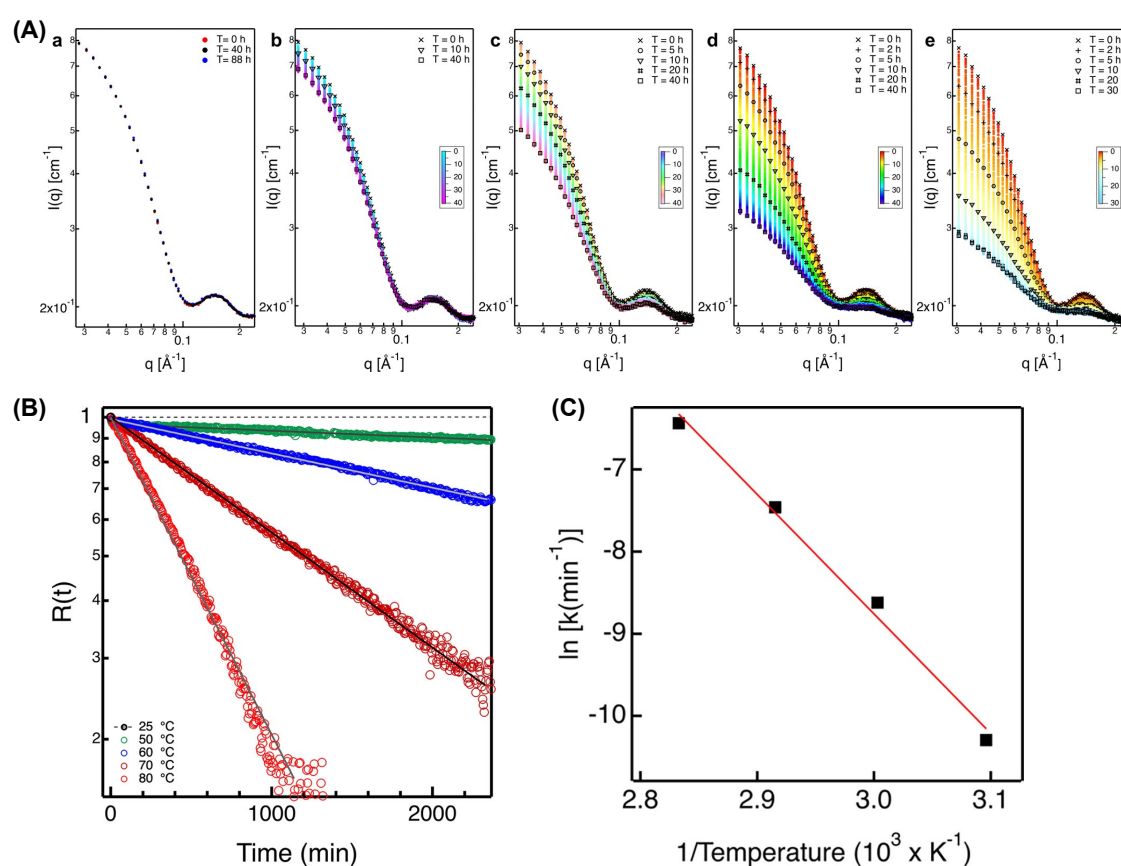


Figure 13. Quantification of interparticle ligand exchange kinetics of thiol ligands on AuNPs using TR-SANS. (A) TR-SANS intensity of Au-hDDT and Au-dDDT mixture at different reaction times at (a) 25, (b) 50, (c) 60, (d) 70, and (e) 80 °C. (B) Normalized relaxation function $R(t)$ vs. time, showing first-order kinetic. (C) Arrhenius plot showing the relationship between the rate constant and temperature for the interparticle ligand exchange reaction. Reproduced with permission [59]. Copyright 2024, American Chemical Society.

6. Conclusions and Outlook

Detailed understanding of nanomaterial surfaces is essential for the rational design of nanomaterials with consistent, predictable, and tailored functions. In this mini review, we discussed traditional and advanced techniques to quantify ligand structure, ligand density, functional groups, and surface reactions on nanomaterials. NMR spectroscopy is a key method to determine the ligand structure on nanomaterials, providing insights into ligand dynamics and ligand-nanoparticle interface through characteristic spectral features such as peak broadening and chemical shifts, which are influenced by the proximity of ligands to the nanomaterial surface. MS, particularly

when combined with advanced analyzers like FTICR, is another powerful tool that can identify ligand structures through fragmentation patterns and molecular ion analysis. Techniques such as X-ray crystallography are used for ordered systems and can solve the complete structure of atomically precise nanoclusters at atomic resolution.

Multiple methods are available to determine ligand density on nanomaterials. TGA is widely used, offering a straightforward estimate of ligand density but is limited regarding structural specificity and sensitivity to impurities. qNMR spectroscopy provides quantitative measurements and is particularly effective for small nanoparticles or when ligands are cleaved for analysis; however, it requires sufficient sample quantities and solubility in the NMR solvent. UV-vis spectroscopy, in conjunction with spectral deconvolution, enables the quantification of mixed ligand systems by resolving overlapping absorption peaks. Advanced techniques such as nanoflow cytometry allow single-particle analysis of ligand densities and accessible ligands, while EELS offers spatial resolution for imaging ligand density variations across single nanomaterials.

Quantification of functional groups on nanomaterials can be done by a variety of methods depending on specific chemical reactivity or physical property. Titration-based techniques apply primarily to acids, bases or ionizable species. Optical assays using dye-based reporters or cleavable probes offer a straightforward way to quantify accessible functional groups by measuring absorbance or emission changes, although steric effects can limit the accuracy. IR and Raman spectroscopy detects molecular vibrations associated with functional groups. NMR spectroscopy and ICP-MS/ICP-OES analyze functional groups by identifying specific elements or structural features for quantification.

Quantifying reactions on nanomaterial surfaces employs methods that can determine reaction kinetics, rates, energetics, and yields. NMR spectroscopy is widely used to analyze reaction products and monitor ligand conversions, and qNMR can further quantify reaction yields. Advanced technique of TR-SANS provides ligand exchange kinetics, rate constants and activation energy of nanomaterial surface reactions.

Each analytical technique has unique strengths and limitations. For example, NMR and MS provide detailed molecular structure information but lack spatial resolution, while techniques like TEM, EELS, and super-resolution microscopy offer high spatial resolution but are less suited for bulk quantification. Given the complexity and heterogeneity of nanomaterials, no single method can address the full range of challenges associated with their characterizations. Employing multiple complementary techniques is therefore recommended to reduce the likelihood of measurement errors or artifacts, to cross-validate, and to ensure reliability of the results. For instance, ligand densities determined by TGA should be validated with qNMR or other spectroscopic methods for potential inclusion of contaminants. As methods for measuring the total functional groups may not accurately reflect the functional groups available for bioconjugation or receptor binding, employing multiple analytical methods such as qNMR and optical reporter probes would provide a more comprehensive quantification of both the total and accessible functional groups for receptor binding.

Beyond molecular structure, functional groups, ligand density, and surface reactions, other important surface characteristics, such as ligand presentation and the ligand-nanomaterial interface, remain poorly understood. Ligand presentation refers to the three-dimensional arrangement of ligands on the nanomaterial surface, including the conformation, spatial orientation and distribution. Factors, such as nanoparticle size, shape, spacer linker length and structure, influence the ligand presentation [60,61], which in turn affects ligand accessibility, reactivity, interactions, and binding strength with receptor molecules in applications like cell targeting. Current analytical techniques generally give the global average. Significant gap exists in the ability to characterize the conformation and spatial orientation of ligands as well as the distribution and spacing of ligands on the nanomaterial surface. Additionally, surface ligands are often in a dynamic equilibrium of various conformations especially in solution. This dynamic behavior is further influenced by interactions between neighboring ligands, adding complexity to the characterization. Furthermore, functional nanomaterials frequently carry multiple ligand types. For instance, nanoparticles for drug delivery are often functionalized with multiple ligands, including antifouling ligands to prevent non-specific protein adsorption and targeting ligands for specific cell type. The presence of different ligand types can lead to complex and ambiguous surface structures, resulting in diverse orientations and binding conformations. Similarly, the precise nature of the ligand-nanomaterial interface, including the bond type (covalent, ionic, hydrogen bonding, or van der Waals interactions), strength, and binding dynamics, also remains poorly understood. For example, in one of the most widely studied systems, thiols on Au, the nature, strength, and mechanism of formation of the Au-S bond under different conditions are still challenging to characterize [62,63]. The ligand-nanomaterial bonding directly impacts the stability of surface ligands with respect to environmental changes in pH, temperature, and ionic strength, which in turn govern the overall stability, reactivity, and properties of the nanomaterial.

The ultimate goal of nanomaterial characterization is to determine the complete structure of the nanomaterial at the molecular and atomic levels, including not only the structures of the core, ligand-nanomaterial interface and

surface ligands, but also the dynamic conformation, spatial orientation and distribution of the surface ligand. For crystallizable atomically precise nanoclusters, single-crystal X-ray diffraction has been successfully used to resolve their total structures and assemblies, including the conformation and arrangement of the ligand shell as well as the interactions between nanoclusters within crystal lattices. However, for heterogeneous nanomaterials, techniques for characterizing nanomaterial surfaces at molecular or atomic levels are lacking. Current microscopy and spectroscopy methods often lack the resolution, surface sensitivity, or scalability required to map ligand distribution or surface heterogeneity at molecular level. Additional challenges include the ability to characterize complex samples and the dynamics of nanomaterial surfaces in different environments. Emerging techniques, such as super-resolution microscopy and single-particle tracking, offer promising avenues for studying nanomaterial surfaces in unprecedented details. Combined with computational modeling and machine learning, these tools could potentially allow precise mapping of nanomaterial surfaces and ligand interactions. Looking forward, integrating conventional analytical and chemical methods with advanced characterization techniques could potentially provide a comprehensive understanding of nanomaterial surfaces with spatial resolution, surface sensitivity, and molecular specificity, facilitating the rational design of nanomaterials for diverse applications.

Author Contributions: M.Y. conceived the concept. H.K. and M.Y. wrote the manuscript draft, edited and approved the final version. All authors have read and agreed to the published version of the manuscript.

Funding: The authors thank partial financial support from the National Science Foundation (CHE-2305006 and CHE-2247574).

Conflicts of Interest: The authors declare no conflict of interest.

References

1. Pozzi, M.; Jonak Dutta, S.; Kuntze, M.; Bading, J.; Rübült, J.S.; Fabig, C.; Langfeldt, M.; Schulz, F.; Horcajada, P.; Parak, W.J. Visualization of the High Surface-to-Volume Ratio of Nanomaterials and Its Consequences. *J. Chem. Educ.* **2024**, *101*, 3146–3155.
2. Liu, P.; Qin, R.; Fu, G.; Zheng, N. Surface Coordination Chemistry of Metal Nanomaterials. *J. Am. Chem. Soc.* **2017**, *139*, 2122–2131.
3. Singh, R.; Srinivas, S.P.; Kumawat, M.; Daima, H.K. Ligand-based surface engineering of nanomaterials: Trends, challenges, and biomedical perspectives. *OpenNano* **2024**, *15*, 100194.
4. Nam, J.-M.; Owen, J.S.; Talapin, D.V. The Ligand–Surface Interface and Its Influence on Nanoparticle Properties. *Acc. Chem. Res.* **2023**, *56*, 2265–2266.
5. Cetin, A.; Ilk Capar, M. Functional-Group Effect of Ligand Molecules on the Aggregation of Gold Nanoparticles: A Molecular Dynamics Simulation Study. *J. Phys. Chem. B* **2022**, *126*, 5534–5543.
6. Shrestha, S.; Wang, B.; Dutta, P. Nanoparticle processing: Understanding and controlling aggregation. *Adv. Colloid Interface Sci.* **2020**, *279*, 102162.
7. Thanh, N.T.K.; Maclean, N.; Mahiddine, S. Mechanisms of Nucleation and Growth of Nanoparticles in Solution. *Chem. Rev.* **2014**, *114*, 7610–7630.
8. An, K.; Somorjai, G.A. Size and Shape Control of Metal Nanoparticles for Reaction Selectivity in Catalysis. *ChemCatChem* **2012**, *4*, 1512–1524.
9. Shi, Y.; Lyu, Z.; Zhao, M.; Chen, R.; Nguyen, Q.N.; Xia, Y. Noble-Metal Nanocrystals with Controlled Shapes for Catalytic and Electrocatalytic Applications. *Chem. Rev.* **2021**, *121*, 649–735.
10. Kumar, S.; Saha, D.; Kohlbrecher, J.; Aswal, V.K. Interplay of interactions for different pathways of the fractal aggregation of nanoparticles. *Chem. Phys. Lett.* **2022**, *803*, 139808.
11. Heuer-Jungemann, A.; Feliu, N.; Bakaimi, I.; Hamaly, M.; Alkilany, A.; Chakraborty, I.; Masood, A.; Casula, M.F.; Kostopoulou, A.; Oh, E.; et al. The role of ligands in the chemical synthesis and applications of inorganic nanoparticles. *Chem. Rev.* **2019**, *119*, 4819–4880.
12. Bhattacharjee, K.; Prasad, B.L.V. Surface functionalization of inorganic nanoparticles with ligands: A necessary step for their utility. *Chem. Soc. Rev.* **2023**, *52*, 2573–2595.
13. Sperling, R.A.; Parak, W.J. Surface modification, functionalization and bioconjugation of colloidal inorganic nanoparticles. *Philos. Trans. A Math. Phys. Eng. Sci.* **2010**, *368*, 1333–1383.
14. Mishra, R.K.; Verma, K.; Singh, D.S. Defect engineering in nanomaterials: Impact, challenges, and applications. *Smart Mater. Manuf.* **2024**, *2*, 100052.
15. Baumler, K.J.; Schaak, R.E. Tutorial on Describing, Classifying, and Visualizing Common Crystal Structures in Nanoscale Materials Systems. *ACS Nanosci. Au* **2024**, *4*, 290–316.
16. Xi, Z.; Zhang, R.; Kiessling, F.; Lammers, T.; Pallares, R.M. Role of Surface Curvature in Gold Nanostar Properties and Applications. *ACS Biomater. Sci. Eng.* **2024**, *10*, 38–50.

17. Walker, D.A.; Leitsch, E.K.; Nap, R.J.; Szleifer, I.; Grzybowski, B.A. Geometric curvature controls the chemical patchiness and self-assembly of nanoparticles. *Nat. Nanotechnol.* **2013**, *8*, 676–681.
18. Pedraza-Tardajos, A.; Claes, N.; Wang, D.; Sánchez-Iglesias, A.; Nandi, P.; Jenkinson, K.; De Meyer, R.; Liz-Marzán, L.M.; Bals, S. Direct visualization of ligands on gold nanoparticles in a liquid environment. *Nat. Chem.* **2024**, *16*, 1278–1285.
19. Sen, S.; Thaker, A.; Sirajudeen, L.; Williams, D.; Nannenga, B.L. Protein–Nanoparticle Complex Structure Determination by Cryo-Electron Microscopy. *ACS Appl. Bio Mater.* **2022**, *5*, 4696–4700.
20. Shevchenko, E.V.; Talapin, D.V.; Kotov, N.A.; O'Brien, S.; Murray, C.B. Structural diversity in binary nanoparticle superlattices. *Nature* **2006**, *439*, 55–59.
21. Zhou, W.; Li, Y.; Partridge, B.E.; Mirkin, C.A. Engineering Anisotropy into Organized Nanoscale Matter. *Chem. Rev.* **2024**, *124*, 11063–11107.
22. Jadzinsky, P.D.; Calero, G.; Ackerson, C.J.; Bushnell, D.A.; Kornberg, R.D. Structure of a Thiol Monolayer-Protected Gold Nanoparticle at 1.1 Å Resolution. *Science* **2007**, *318*, 430–433.
23. Li, Y.; Jin, R. Seeing Ligands on Nanoclusters and in Their Assemblies by X-ray Crystallography: Atomically Precise Nanochemistry and Beyond. *J. Am. Chem. Soc.* **2020**, *142*, 13627–13644.
24. Marbella, L.E.; Millstone, J.E. NMR Techniques for Noble Metal Nanoparticles. *Chem. Mater.* **2015**, *27*, 2721–2739.
25. Jayawardena, H.S.N.; Liyanage, S.H.; Rathnayake, K.; Patel, U.; Yan, M. Analytical Methods for Characterization of Nanomaterial Surfaces. *Anal. Chem.* **2021**, *93*, 1889–1911.
26. Wu, M.; Vartanian, A.M.; Chong, G.; Pandiakumar, A.K.; Hamers, R.J.; Hernandez, R.; Murphy, C.J. Solution NMR Analysis of Ligand Environment in Quaternary Ammonium-Terminated Self-Assembled Monolayers on Gold Nanoparticles: The Effect of Surface Curvature and Ligand Structure. *J. Am. Chem. Soc.* **2019**, *141*, 4316–4327.
27. Novotný, J.; Vicha, J.; Bora, P.L.; Repisky, M.; Straka, M.; Komorovsky, S.; Marek, R. Linking the Character of the Metal–Ligand Bond to the Ligand NMR Shielding in Transition-Metal Complexes: NMR Contributions from Spin–Orbit Coupling. *J. Chem. Theory Comput.* **2017**, *13*, 3586–3601.
28. Vicha, J.; Novotný, J.; Komorovsky, S.; Straka, M.; Kaupp, M.; Marek, R. Relativistic Heavy-Neighbor-Atom Effects on NMR Shifts: Concepts and Trends Across the Periodic Table. *Chem. Rev.* **2020**, *120*, 7065–7103.
29. Ndugire, W.; Liyanage, S.H.; Yan, M. Carbohydrate-Presenting Metal Nanoparticles: Synthesis, Characterization and Applications. In *Comprehensive Glycoscience*, 2nd ed.; Barchi, J.J., Ed.; Elsevier: Amsterdam, The Netherlands, 2021; pp. 380–405.
30. Wu, Z.; Jin, R. Stability of the Two Au–S Binding Modes in Au₂₅(SG)₁₈ Nanoclusters Probed by NMR and Optical Spectroscopy. *ACS Nano* **2009**, *3*, 2036–2042.
31. Ghosh, J.; Cooks, R.G. Mass spectrometry in materials synthesis. *Trends Anal. Chem.* **2023**, *161*, 117010.
32. Comby-Zerbino, C.; Dagany, X.; Chirot, F.; Dugourd, P.; Antoine, R. The emergence of mass spectrometry for characterizing nanomaterials. Atomically precise nanoclusters and beyond. *Mater. Adv.* **2021**, *2*, 4896–4913.
33. Nicolardi, S.; van der Burgt, Y.E.M.; Codée, J.D.C.; Wuhler, M.; Hokke, C.H.; Chiodo, F. Structural Characterization of Biofunctionalized Gold Nanoparticles by Ultrahigh-Resolution Mass Spectrometry. *ACS Nano* **2017**, *11*, 8257–8264.
34. Smith, A.M.; Johnston, K.A.; Crawford, S.E.; Marbella, L.E.; Millstone, J.E. Ligand density quantification on colloidal inorganic nanoparticles. *Analyst* **2017**, *142*, 11–29.
35. Mansfield, E.; Tyner, K.M.; Poling, C.M.; Blacklock, J.L. Determination of Nanoparticle Surface Coatings and Nanoparticle Purity Using Microscale Thermogravimetric Analysis. *Anal. Chem.* **2014**, *86*, 1478–1484.
36. Choi, K.; Myoung, S.; Seo, Y.; Ahn, S. Quantitative NMR as a Versatile Tool for the Reference Material Preparation. *Magnetochemistry* **2021**, *7*, 15.
37. Kong, N.; Zhou, J.; Park, J.; Xie, S.; Ramström, O.; Yan, M. Quantitative Fluorine NMR To Determine Carbohydrate Density on Glyconanomaterials Synthesized from Perfluorophenyl Azide-Functionalized Silica Nanoparticles by Click Reaction. *Anal. Chem.* **2015**, *87*, 9451–9458.
38. Potts, J.C.; Jain, A.; Amabilino, D.B.; Rawson, F.J.; Pérez-García, L. Molecular Surface Quantification of Multifunctionalized Gold Nanoparticles Using UV–Visible Absorption Spectroscopy Deconvolution. *Anal. Chem.* **2023**, *95*, 12998–13002.
39. Senoner, M.; Unger, W.E.S. SIMS imaging of the nanoworld: Applications in science and technology. *J. Anal. At. Spectrom.* **2012**, *27*, 1050–1068.
40. Eller, M.J.; Chandra, K.; Coughlin, E.E.; Odom, T.W.; Schweikert, E.A. Label Free Particle-by-Particle Quantification of DNA Loading on Sorted Gold Nanostars. *Anal. Chem.* **2019**, *91*, 5566–5572.
41. Masuko, T.; Minami, A.; Iwasaki, N.; Majima, T.; Nishimura, S.-I.; Lee, Y.C. Carbohydrate analysis by a phenol–sulfuric acid method in microplate format. *Anal. Biochem.* **2005**, *339*, 69–72.
42. Wang, X.; Ramström, O.; Yan, M. A photochemically initiated chemistry for coupling underivatized carbohydrates to gold nanoparticles. *J. Mater. Chem.* **2009**, *19*, 8944–8949.
43. Janicek, B.E.; Hinman, J.G.; Hinman, J.J.; Bae, S.H.; Wu, M.; Turner, J.; Chang, H.-H.; Park, E.; Lawless, R.; Suslick,

- K.S.; et al. Quantitative Imaging of Organic Ligand Density on Anisotropic Inorganic Nanocrystals. *Nano Lett.* **2019**, *19*, 6308–6314.
44. Chen, C.; Zhou, Y.; Chen, C.; Zhu, S.; Yan, X. Quantification of Available Ligand Density on the Surface of Targeted Liposomal Nanomedicines at the Single-Particle Level. *ACS Nano* **2022**, *16*, 6886–6897.
 45. Geißler, D.; Nirmalanathan-Budau, N.; Scholtz, L.; Tavernaro, I.; Resch-Genger, U. Analyzing the surface of functional nanomaterials—How to quantify the total and derivatizable number of functional groups and ligands. *Microchim. Acta* **2021**, *188*, 321.
 46. Kunc, F.; Balhara, V.; Brinkmann, A.; Sun, Y.; Leek, D.M.; Johnston, L.J. Quantification and Stability Determination of Surface Amine Groups on Silica Nanoparticles Using Solution NMR. *Anal. Chem.* **2018**, *90*, 13322–13330.
 47. Kunc, F.; Balhara, V.; Sun, Y.; Daroszewska, M.; Jakubek, Z.J.; Hill, M.; Brinkmann, A.; Johnston, L.J. Quantification of surface functional groups on silica nanoparticles: Comparison of thermogravimetric analysis and quantitative NMR. *Analyst* **2019**, *144*, 5589–5599.
 48. Moser, M.; Nirmalanathan, N.; Behnke, T.; Geißler, D.; Resch-Genger, U. Multimodal Cleavable Reporters versus Conventional Labels for Optical Quantification of Accessible Amino and Carboxy Groups on Nano- and Microparticles. *Anal. Chem.* **2018**, *90*, 5887–5895.
 49. Roloff, A.; Nirmalanathan-Budau, N.; Rühle, B.; Borchering, H.; Thiele, T.; Schedler, U.; Resch-Genger, U. Quantification of Aldehydes on Polymeric Microbead Surfaces via Catch and Release of Reporter Chromophores. *Anal. Chem.* **2019**, *91*, 8827–8834.
 50. Sun, Y.; Kunc, F.; Balhara, V.; Coleman, B.; Kodra, O.; Raza, M.; Chen, M.; Brinkmann, A.; Lopinski, G.P.; Johnston, L.J. Quantification of amine functional groups on silica nanoparticles: A multi-method approach. *Nanoscale Adv.* **2019**, *1*, 1598–1607.
 51. Konsolakis, M. Surface Chemistry and Catalysis. *Catalysts* **2016**, *6*, 102.
 52. Somorjai, G.A.; Li, Y. *Introduction to Surface Chemistry and Catalysis*, 2nd ed.; Wiley: New York, NY, USA, 2010.
 53. Sanità, G.; Carrese, B.; Lamberti, A. Nanoparticle surface functionalization: How to improve biocompatibility and cellular internalization. *Front. Mol. Biosci.* **2020**, *7*, 587012.
 54. Ndugire, W.; Yan, M. Synthesis and solution isomerization of water-soluble Au₉ nanoclusters prepared by nuclearity conversion of [Au₁₁(PPh₃)₈Cl₂]Cl. *Nanoscale* **2021**, *13*, 16809–16817.
 55. Klein, K.; Loza, K.; Heggen, M.; Epple, M. An efficient method for covalent surface functionalization of ultrasmall metallic nanoparticles by surface azidation followed by copper-catalyzed azide-alkyne cycloaddition (click chemistry). *ChemNanoMat* **2021**, *7*, 1330–1339.
 56. Yang, X.; Chen, F.; Kim, M.A.; Liu, H.; Wolf, L.M.; Yan, M. Using metal substrates to enhance the reactivity of graphene towards Diels–Alder reactions. *Phys. Chem. Chem. Phys.* **2022**, *24*, 20082–20093.
 57. Tu, J.; Yan, M. Enhancing the chemical reactivity of graphene through substrate engineering. *Small* **2024**, e2408116.
 58. Calvin, J.J.; Sedlak, A.B.; Brewer, A.S.; Kaufman, T.M.; Alivisatos, A.P. Evidence and Structural Insights into a Ligand-Mediated Phase Transition in the Solvated Ligand Shell of Quantum Dots. *ACS Nano* **2024**, *18*, 25257–25270.
 59. Lee, S.-J.; Jang, J.D.; Choi, S.-M. Interparticle Ligand Exchange Kinetics Revealed by Time-Resolved SANS. *Nano Lett.* **2025**, *25*, 981–986.
 60. Wang, X.; Ramström, O.; Yan, M. Quantitative Analysis of Multivalent Ligand Presentation on Gold Glyconanoparticles and the Impact on Lectin Binding. *Anal. Chem.* **2010**, *82*, 9082–9089.
 61. Wang, X.; Ramström, O.; Yan, M. Glyconanomaterials: Synthesis, Characterization, and Ligand Presentation. *Adv. Mater.* **2010**, *22*, 1946–1953.
 62. Rashid, U.; Bro-Jørgensen, W.; Harilal, K.B.; Sreelakshmi, P.A.; Mondal, R.R.; Chittari Pisharam, V.; Parida, K.N.; Geetharani, K.; Hamill, J.M.; Kaliginedi, V. Chemistry of the Au–Thiol Interface through the Lens of Single-Molecule Flicker Noise Measurements. *J. Am. Chem. Soc.* **2024**, *146*, 9063–9073.
 63. Inkpen, M.S.; Liu, Z.F.; Li, H.; Campos, L.M.; Neaton, J.B.; Venkataraman, L. Non-chemisorbed gold–sulfur binding prevails in self-assembled monolayers. *Nat. Chem.* **2019**, *11*, 351–358.